Chapter 12

Segmented-Aperture Telescopes

12.1 Introduction

Astronomers require larger and larger radiation-gathering apertures for their telescopes to penetrate farther into the mysteries of the universe. Large telescopes collect more photons and thus see fainter objects. These large apertures also increase the angular resolution across the object, as we saw in Chapter 10. For practical reasons such as telescope mass and thermal inertia, astronomers who build ground-based telescopes now partition primary mirrors greater than about 8 m into smaller segments, with each segment aligned so that its surfaces fall on the desired concave surface of the larger mirror.

Large space- and ground-based telescopes are often divided into two stages. Stage 1 is the large collector, which forms an imperfect image in complex amplitude and phase. Before an image is detected, stage 2 of the optical system takes this imperfect image and removes wavefront aberrations using WFSC. This principle was discussed in Chapter 11. In Chapter 5 we learned that the number of reflections in the optical system needs to be small in order to minimize the power that is absorbed by the mirrors and that does not reach the focal plane. Consequently, rather than correcting the wavefront at an image of the telescope pupil, many telescopes correct the wavefront at the secondary mirror of the astronomical telescope before the primary focus.[1,2] Correcting the wavefront at the secondary limits the FOV of the telescope that can be corrected. However, most astronomical applications today use a narrow FOV (limited by the expensive digital array detector size or by atmospheric turbulence), so wavefront control (WFC) at the secondary is sufficient.

Frequently, the optical system for large telescopes is divided into three parts: the large precision telescope radiation collector, a metrology and WFSC system (see Chapter 11), and the instrument that analyzes the radiation. The motivation behind this configuration is to reduce the cost of the telescope system. For ground-based telescopes, the two expensive subsystems are the dome and the very stiff massive mechanical structure required to hold the mirror, the secondary, and its supports. This support structure is necessary because in order

to point at celestial objects for long integration times, the telescope needs to track across the sky, counteracting the earth's rotation. During this tracking, the gravity vector changes continuously. For space telescopes, the volume of the launch vehicle is more of a constraint than is the mass. New large space telescopes are being designed to have deployable mirrors and a deployable metering structure. Partitioning telescope systems into these three sections results in less-expensive telescopes per unit of capability.[3]

This chapter provides an analysis of the segmented-aperture telescope and shows how two-stage or adaptive optics mitigates unwanted errors and improves image quality. In two-stage optics, the first stage delivers an aberrated image to the second optical system, which corrects for wavefront aberrations to deliver a near-diffraction-limited image with the required FOV. Also discussed are performance limits to segmented apertures. An analysis of the HST wavefront error (WFE) is used as the basis for a discussion.

Segmented apertures that fold for packaging, deploy, and align themselves robotically after launch are needed for space telescopes larger than approximately a 4-m aperture. The JWST has a 6.5-m aperture, is currently (as of 2012) under construction, and will be the first space telescope to be segmented, deployed, and aligned robotically.

Each segmented-aperture telescope is unique. Four modern segmented telescopes are under construction. These are the space-based JWST and the new very large ground-based telescopes: the TMT, the E-ELT, and the Giant Segmented Mirror Telescope (GSMT). Several ground-based segmented telescopes are in successful operation. These are the Keck twin 10-m telescopes, the 9.2-m Hobby Eberly Telescope (HET), and the 10.4-m Gran Telescopio Canarias (GTC). The Large Binocular Telescope (LBT) is a unique segmented telescope in that it is a 23-m-diameter sparse-aperture telescope consisting of two 8-m-diameter mirrors on one telescope mount. In the next section, we examine the way in which two-stage optics was applied to the HST and use this example to show how two-stage optics are applied to segmented telescopes.

12.2 Two-Stage Optics Applied to Continuous Primary Mirrors

The principles of two-stage optics are discussed in this section, and an analysis of the calculated WFC as a function of FOV and demagnification is provided. If both the FOV and the WFC are small, the WFC can be applied at any convenient surface in the system. For example, astronomers successfully use active secondary mirrors on Cassegrain and Ritchey–Chrétien telescopes.[4,5] Here we first consider two-stage optics as applied to continuous sheet mirrors, and then as applied to two-stage optics[6] for a segmented primary telescope.

12.2.1 Monolithic mirrors

The most frequently encountered WFE on a figured optical surface occurs when the error has slowly varying departures from the ideal. Correction of this WFE is done at an exit pupil, which appears in the second stage. In general, this pupil is

much smaller than the entrance pupil of the system. The WFC at the exit pupil requires the wavefront amplitude (piston) to be exactly the same as the wavefront amplitude of the WFE. However, the correction is placed on a much-smaller-diameter image of the pupil than the entrance pupil (primary mirror) of the telescope. Consequently, the wavefront slopes are increased. The wavefront slopes are increased by the ratio of the pupil diameter on the corrector to the entrance pupil diameter.

When the WFC is placed on a much smaller optical surface, three geometrical limitations to the performance are introduced:

1. Magnification difference of the image of the first-stage error with respect to the wavefront-corrector surface is increased. For example, for the Wide-Field Planetary Camera (WF/PC) in the HST, the image of the entrance pupil (the 2.4-m primary mirror) is demagnified to 1 cm in diameter.

2. Wavefront quality is highly dependent on pupil decentering, so errors are very sensitive to a mechanical shear or lateral displacement of the image of the pupil on the corrective element and the centration of the corrector on the system axis. A closed-loop adaptive optics system quickly runs out of dynamic range if asked to correct for these decentering errors.

3. An optical path for oblique rays caused by diffraction spillover occurs in the far IR to limit the performance of telescopes that use segmented mirrors.

We will calculate the errors on the wavefront that are due to magnification differences in the image of the first stage with respect to the wavefront-corrector surface and calculate the effects of pupil decentering.

Let us recall that third-order Seidel aberrations are defined as follows: The equation for the complex amplitude of a spherical electromagnetic wave converging to a point a distance f from the pupil (lens) is given by Eq. (4.15):

$$u'(x,y) = u(x,y)\exp\left\{-j\frac{k}{2f}\left(x^2 + y^2\right)\right\},\qquad(12.1)$$

where $k = 2\pi/\lambda$, and x and y are coordinates across the pupil plane. We represent the exponent in the above equation as

$$E(x,y) = -j\frac{k}{2f}\left(x^2 + y^2\right)\left[1 + W(x,y)\right],\qquad(12.2)$$

where $W(x,y)$ is the deviation of the wavefront from a sphere (wavefront aberration). We show that wavefront aberration is the normalized deviation, or error, on a reference spherical wave. In Chapter 4 we saw that wave aberration is

a function of two sets of coordinates. One set is that of the exit pupil plane, the other that of the image plane. In Chapter 4, we also defined the Seidel aberrations as an expansion of the WFE *W* in terms of parameters in the image plane and the pupil plane, as follows [Eq. (4.17)]:

$$W = \sum_{k,n,m} a_{knm} h^k \cdot \rho^n \cdot \left(\cos\psi \right)^m, \qquad (12.3)$$

where:

  a_{knm} is the normalized aberration coefficient,
  h is the normalized height in the image plane $0 \le h \le 1$,
  ρ is the normalized height in the pupil plane $0 \le \rho \le 1$, and
  ψ is the angle between the meridional plane and the plane formed by h, ρ,
  and the axis.

Aberration terms contain the set of coefficients for which the integers $N = k + n - 1$, where N is the order of the aberration. Using the expression in Eq. (12.3), we obtain the third-order monochromatic waveform aberration terms:

$$\begin{aligned} W = \left(a_{040} \cdot \rho^4 \right) + \left(a_{131} \cdot h \cdot \rho^3 \cdot \cos\psi \right) + \left(a_{222} h^2 \cdot \rho^2 \cos^2\psi \right) \\ + \left(a_{220} \cdot h^2 \cdot \rho^2 \right) + \left(a_{311} \cdot h^3 \cdot \rho \cdot \cos\psi \right). \end{aligned} \qquad (12.4)$$

In Eq. (12.4), the first three terms represent the deviation of the wavefront from a sphere. The last two terms relocate the center of the wavefront. Each of these terms has a common name, shown in Table 12.1.

   In the two-stage optics system, where the entrance pupil (primary mirror) is imaged onto an optical element used for correcting aberrations, unwanted spherical aberration is introduced if one is not careful. A difference in scale between the image of the entrance pupil and the WFE placed on the exit pupil introduces spherical aberration. In the case of pure spherical aberration, for the WFE in the *y* direction, we have $W_{040} = a_{040} y^4$.

   If the image of the pupil is not of the same scale as that for the correcting element, then in place of having the same radial dependence, the correction on

Table 12.1 Five third-order Seidel aberrations with their functional relationship to physical properties of an optical system.

Spherical aberration	$a_{040}\rho^4$
Coma	$a_{131}h\rho^3\cos\psi$
Astigmatism and field curvature	$a_{222}h^2\rho^2\cos^2\psi + a_{220}h^2\rho^2$
Distortion	$a_{311}h^3\rho\cos\psi$

the exit pupil is given by $W = a_{040}(1+\varepsilon)^4 \cdot y^4$, where ε is an additive error term on the scale of the radius. Since $\varepsilon \ll 1$, the resulting error is given by $W = a_{040}4\varepsilon y^4$. Thus, there is some residual spherical aberration. In general, this scale error can be made small by control of the curvatures and separations of the mirrors.

Pupil shearing is far more damaging to image quality and results from the entrance pupil being decentered on the WFC element located at the image of the pupil. The magnitude of the error is more difficult to control since it depends on the state of collimation of the optical train. If the amount of correction is large, it is very important to have the corrective element exactly centered on the image of the surface where the error is located.

Let us examine the case of an error in pure spherical aberration $W = a_{040}y^4$. When the corrective surface is of equal magnitude but displaced by a transverse distance Δy, it is subtracted, as shown in Fig. 12.1. We then have the relationship for the spherical aberration due to pupil shear:

$$W = a_{040}y^4 - a_{040}\left(y - \Delta y\right)^4. \tag{12.5}$$

Since $\Delta y \gg \left(\Delta y\right)^2$, we neglect the terms in the expansion beyond Δy and obtain

$$\Delta W = a_{040}y^4 - a_{040}\left(y^4 - 4y^3\Delta y + \ldots\right) = 4a_{040}y^3\Delta y, \tag{12.6}$$

which is coma, or

$$W_{131} = 8a_{040}y^3\Delta y. \tag{12.7}$$

This coma is not field dependent and is constant over the entire field of a given system. The important quantity is the ratio of the residual W_{131} error to the first-stage input error W_{040}:

$$\frac{W_{131}}{W_{040}} = \frac{8ay^3\Delta y}{ay^4} = 8\left(\frac{\Delta y}{y}\right). \tag{12.8}$$

Solving for Δy, we obtain

$$\Delta y = \left(\frac{W_{131}}{W_{040}}\right) \cdot \frac{y}{8}. \tag{12.9}$$

The corrective elements need to be aligned accurately with respect to the axis to obtain negligible aberration. The image of the telescope pupil needs to be centered on the corrective element. The relay optics in the WF/PC are aligned by

superposing the axes of the primary and secondary mirrors. The WF/PC is aligned to the telescope by superposing the axis of the WF/PC to the axis of the telescope. If this alignment is perfect, an image of the HST telescope pupil appears superposed on the secondary in the relay telescopes, which is the corrective element. If there is a shear between the image of the aberrated pupil and the corrective element, the aberration in the telescope can be made worse than it would be by simply not correcting the spherical aberration.

Figure 12.1 shows a plot of the magnitude of the aberration as a function of normalized lateral translation or shear for spherical aberration. The dashed line in the figure has been sheared relative to the solid line. The solid line represents the error on the primary mirror requiring correction, and the dashed line represents the magnitude of the aberration placed intentionally on the correcting element. The aberration magnitude on the correcting element (dashed line) has a sign opposite to that of the error on the primary mirror. Figure 12.2 plots the
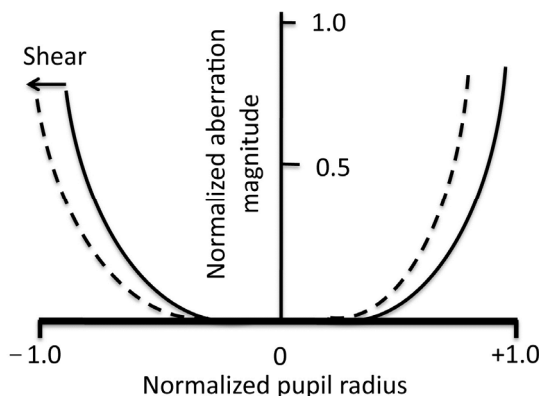
Figure 12.1 Plot of the normalized radius (not FOV) at the pupil plane as a function of the magnitude of aberration for spherical aberration (W_{040}).
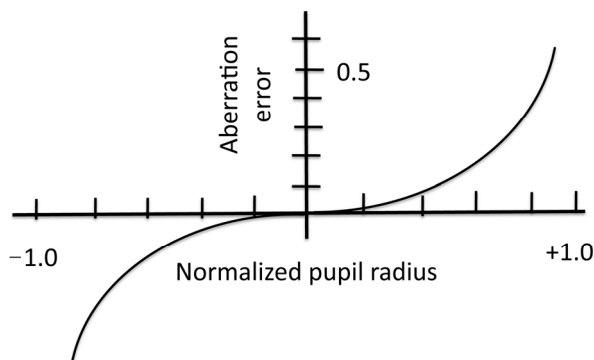
Figure 12.2 Plot showing the effect of shear between the image of the pupil and the wavefront-correcting element. (Reprinted with permission from Ref. 6.)

difference between the two curves in Fig. 12.1 (dashed curve minus solid curve) to show that lateral shear error introduces unwanted coma aberration. At the top of Fig. 12.2, we see the fourth-order error (spherical aberration) and the shifted fourth-order corrector. The axes of the two are not collinear but rather parallel and shifted one relative to the other. In the lower plot we see the difference between the two; i.e., the residual that remains uncorrected is the characteristic asymmetric aberration of coma.

Raytrace design for the WF/PC showed that alignment within a few microns was necessary.[7] Therefore, the optical axis of the new WF/PC assembly launched on the first HST servicing mission needed to be aligned to the telescope to within a few microns. The latches that held the WF/PC into the optical telescope assembly (OTA) were only accurate to within a few thousandth of an inch, far too imprecise for any aberration correction to work. It was necessary to use electrostrictive actuators on one of the fold mirrors internal to the WF/PC in order to correctly align the axis of the OTA with the axis of the WF/PC. Details of this correction are given in the next section.

12.2.2 Correcting the Hubble Space Telescope

An example of the application of two-stage optics is found in the correction of the HST. The telescope could not have been brought back to earth to refigure the primary mirror. However, the telescope was able to be captured by the Space Shuttle and brought back to the large shuttle bay, and the instruments swapped out for new ones. The WF/PC camera was therefore accessible using extravehicular activity by astronauts. The original WF/PC was designed to be replaced as technology improved. The WF/PC was redesigned, and a new one built with corrective optics inside the instrument.

The first flight system that used these principles was the HST. Unfortunately, the telescope was launched with –6.6 waves of error at 0.63 μm of spherical aberration over its 2.4-m diameter. Astronomers knew that the sensitivity of detectors would improve over time and that science measurement priorities would change over time. Therefore, the WF/PC was designed to be replaced with upgraded components on later HST servicing missions. The WFE on the primary mirror was corrected using new optical components in a second camera that was built to replace the camera that was launched with the aberrated telescope. The principles of two-stage optics were applied in building the second WF/PC, called WF/PC2, which corrected the aberration on the primary mirror of the HST.
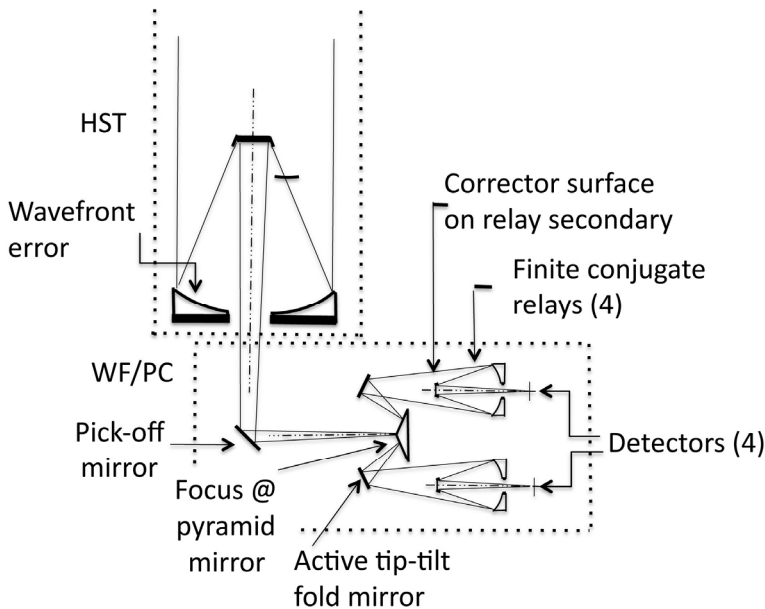
Figure 12.3 gives a schematic view of the HST to show the fore-optics, the pyramid mirror located at the Ritchey−Chrétien focus, and the WF/PC, and identifies the location within the WF/PC where the wavefront corrector was added. The OTA is shown in the dotted box in the upper left of the figure. The WF/PC is shown in this figure to be inside the dotted box in the lower center of the figure. The HST primary mirror error was measured while the telescope was on orbit and, as mentioned above, was determined to be –6.6 waves at 633 nm of spherical aberration. The minus sign refers to the fact that the marginal ray crosses the axis at a distance from the vertex of the primary mirror that is greater

than the distance to the paraxial focus. Opticians call this *overcorrected*, meaning that the outer portions of the mirror were figured to be flatter than needed.

Figure 12.3 also shows the four optical systems in the WF/PC that relay the complex amplitude and phase at the image plane into four focal plane detectors. These four relay systems have a finite distance to the objects (this distance is the image plane of the HST) and a finite distance to the image on the focal plane detector. Therefore, the relay systems are called finite conjugate relays. At the pyramid mirror, the FOV is divided into four sections, and each section is then relayed through its own small optical system and focused onto a special-purpose CCD. There are four relay primaries, secondaries, and focal planes in the WF/PC. The radius y of the secondary mirrors within the WF/PC relay optics is approximately 7.5 mm. We assume that the allowable amount of coma is 0.2 waves. Then, the required placement of the image of the primary mirror (which is the exit pupil of the OTA on the secondary mirror) is given by

$$\Delta y = 28 \ \mu\text{m}, \tag{12.10}$$

where, we have inserted $W_{131} = 0.2$ waves, $W_{040} = 6.6$ waves, and $y = 7500 \ \mu\text{m}$ into Eq. (12.9).

Figure 12.3 Schematic view of the HST and the WF/PC. Light enters the HST from above, strikes the primary mirror, and reflects from the secondary and the tertiary (pick-off mirror) to an image plane. The image plane falls onto a four-sided pyramid, which divides the image into four quadrants. Each face of the pyramid mirror has four slightly concave mirrors. Each quadrant of the image is reflected into four finite conjugate relay Cassegrain telescope assemblies. The image plane provided by the OTA, shown inside the dotted box on the upper left, is divided into four parts within the WF/PC instrument, and each part is sent to one of four relay cameras and reimaged onto an 800×800-pixel CCD focal plane.

Therefore, as a result of the –6.6-wave error on the primary mirror, the camera system designed to replace the first WF/PC needed to have its axis co-aligned with the axis of the OTA to within a tolerance of 28 μm. This is a tighter tolerance for placement of the exit pupil of the OTA than was originally specified.

The conclusion is that in the presence of the large W_{040} error, a small displacement of the exit pupil on the corrective mirror produces significant coma. This coma is constant over the field of a single camera but different for other WF/PCs, depending on their pupil position errors. A similar error arises when any corrective surface is sheared with regard to another surface. The sensitivity depends on the slope of the error wavefront and can be readily evaluated for any specific error surface in a similar manner as was described above.

If the primary mirror of the OTA has no figure error, then the WF/PC needs to be aligned to only a few tens of mm. The tolerance to match the axis of each camera within the new WF/PC to the OTA with the –6.6 waves of spherical aberration exceeded the tolerance available on the telescope radial latches. That problem was solved using an adaptive tip/tilt mirror as the fold mirror in the WF/PC, shown schematically in Fig. 12.3. The first images recorded with the camera showed slight misalignment. Star images were recorded. The magnitude and sign of the tilt error were calculated using prescription retrieval on the star images recorded across the FOV and through focus. The amount of tip and tilt needed to correct the misalignment was calculated and transmitted to the telescope, and one adjustment was made. Excellent images were then recorded, and the system was never adjusted again during the 15-year orbital lifetime of the camera.

12.3 Two-Stage Optics Applied to Segmented Primary Mirrors

12.3.1 Introduction

A segmented primary mirror is used for several reasons:

1. A single monolithic mirror is too heavy for a cost-effective ground or space telescope.
2. The telescope needs to fold up to occupy a smaller volume for those launch vehicles that are volume-shroud constrained.
3. Fabrication of the large primary mirror can be achieved with ease and speed.

Ground-based segmented telescopes employ lightweight segments and use optical metrology and WFSC to add the stiffness and stability required to maintain the image quality requirements. To create a single large primary mirror, the reflecting surfaces' smaller mirrors are optically figured so that each can be placed with its surface superposed to much less than the wavelength of light onto the virtual surface of the desired parent telescope surface.

Two pupil geometries are used for segmenting a primary telescope mirror. One is in petals (or keystones), which uses segments that are slices in azimuthal

and radial coordinates. Keystone petals were used during the 1980s (before Keck) to demonstrate that a large-aperture (4-m) mirror could be segmented and controlled to the high accuracy needed for imaging.[8] The other geometry uses close-packed hexagons. Two pupils that are segmented with these geometries are shown in Fig. 12.4.

With no central segment, the number of segments as a function of the number of rings K_{rings} is given by $K_{segments} = 3K_{rings} (K_{rings} + 1)$. The side length l of the hexagon required for an equivalent area circular diameter area D is given by[9]

$$l = D\sqrt{\frac{\pi}{6\sqrt{3} \cdot K_{segments}}}. \tag{12.11}$$

If the primary mirror is spherical, then all of the segments are identical and interchangeable, given that the support structures on the back share symmetry. If the primary mirror is not spherical, then the optical prescription figured into the segments depends on the distance from the vertex of the parent primary mirror. If the primary mirror is not spherical, but rather represented by a conic, then the number of different optical surfaces is $K_{segments}/6$. Note that the surfaces of some segments differ in orientation, rather than in distance from the vertex. Table 12.2 gives the number of segments, surface types, position actuators, and edge sensors as a function of the number of rings (up to 5 rings).[9] These dimensions are calculated for a segmented flat mirror. A telescope mirror is a doubly curved or "cupped" surface. The length of the edges for a segmented mirror assembly that is doubly curved depends[10] on the system F-number.

(a)   (b)
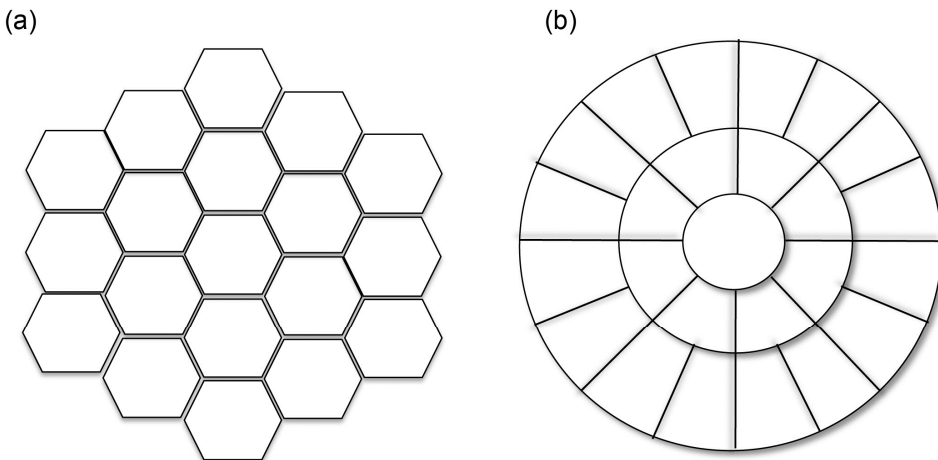
Figure 12.4 Illustration showing two segmented pupils: (a) the close-packed hexagon and (b) the keystones.

Table 12.2 Segmented mirror parameters as a function of the number of rings. Entries in this table assume two sensors per edge.

Rings	1	2	3	4	5
Segments	6	18	36	60	90
Surface types	1	3	6	10	15
Position actuators	18	54	108	180	270
Edge sensors	12	72	168	300	492

12.3.2 Large deployable reflector

The concept for two-stage optics was developed in response to the need for a large deployable reflector (LDR) for IR astronomy. The drawing in Fig. 12.5 shows the concept of the LDR. The term *two-stage optics* applies in cases in which the large primary mirror is passive and the resulting degraded image in the first focus (the first stage) is accepted. The second, much smaller stage upgrades this WFE by active or passive techniques.
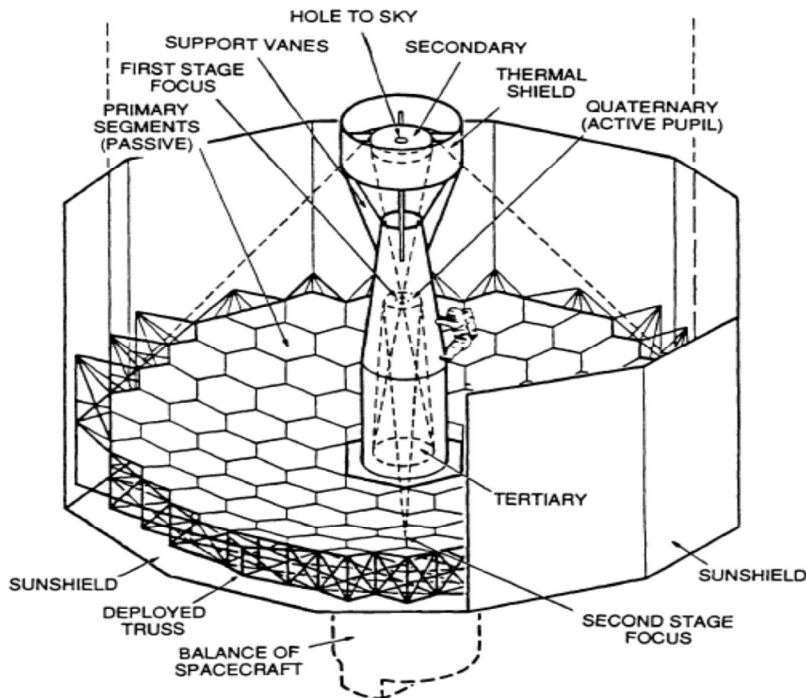
Figure 12.5 Perspective view of the large deployable reflector telescope utilizing the two-stage optics. The first stage comprises the large primary mirror and the secondary mirror. The focus of the first stage is located at a hole in the active quaternary. The beam expands to fill the tertiary mirror and reflects from the surface of the quaternary mirror. The optical power on the elements is adjusted to map the deeply curved primary mirror onto the flat quaternary, which is an active mirror and is used for correcting the wavefront and the tip-tilt piston errors in the segments on the primary. (Reprinted with permission from Ref. 6.)

12.4 Alignment and Manufacturing Tolerances for Segmented Telescopes

Similar to the JWST, the next-generation large-aperture space telescope for optical and UV astronomy has a segmented large deployable primary mirror of 8 to 16 m.[11,12] The astronomer and the optical engineer need to decide how much control authority for the wavefront is on the primary mirror and how much system control authority can be assigned to a second stage of the optical system and thus onto an active or adaptive optics element. Holding and tracking the motion of the primary mirror to a tolerance of 5 nm over a 16-m aperture for diffraction-limited performance in the UV is very difficult and extremely expensive. The telescope designer needs to perform a cost-benefit trade-off study to decide how resources are to be divided between a large segmented primary mirror and the smaller surface on an adaptive optics mirror. Factors that influence this design decision are discussed in this section.

The surface of each mirror segment of a segmented primary mirror must lie on the surface of the desired primary mirror optical prescription. However, each segment is mechanically independent from the others, connected only through a mechanical back plane structure that supports and aligns each individual mirror segment. Adjustments are needed for tip, tilt, piston, off-axis positions, and rotations of each segment. Piston is generally considered along the direction of the ray to the image plane. Some segmented-mirror telescopes use segments with spherical surfaces, which relieve the tolerance of axial position. However, high-quality imaging telescopes, such as the two Keck 10-m telescopes, have an aspheric surface for the primary mirror; therefore, each mirror segment is an aspheric surface with the optical axis off of the surface. These segments with aspheric surfaces require careful alignment.[13–16] The radii of curvaturesof each of the segments must be within a particular tolerance. The value of this tolerance is discussed in the following section.

12.4.1 Curvature manufacturing tolerance

We examine a simple two-segment mirror to describe the tolerances necessary to obtain diffraction-limited performance. To align a segmented aperture, the axes of each segment must be collinear with the axis of the reference conic surface, which passes through the desired focal point, as shown in Fig. 12.6. The reference conic surface is a surface in space on which the surface of each segment is placed to form the primary mirror of the telescope. Recall that all conic surfaces have an axis defined by the line from the vertex of the surface through the focus point.

To calculate the allowable error on the collinearity of the segment axes, we need to imagine that each segment creates its own independent (uncorrelated) image. That is, the angular resolution at the focal plane corresponds to that from only one segment. Next, we bring the axes together and match the radii of curvature of each segment so that an image is formed at the angular resolution of the full aperture across the desired FOV of the system of mirrors that form the

segmented primary. The wavefront from each segment is now coherent with that from its neighboring segment, and a high-resolution image is formed.

As the FOV becomes larger, the tolerance to match the radii of curvature becomes tighter to maintain diffraction-limited performance across the field.[17] This can be seen intuitively. The plate scale at the focal plane (for example, in units of seconds of arc per micron) depends on the focal length. The longer the focal length, the larger the image is. Each segment superposes its own image onto that of the others, and we need the image scale and thus the focal lengths to be matched within a certain tolerance.

Figure 12.7 shows a pupil plane of diameter D and two image planes. One image plane, indicated by focal length f_1, is shorter than the second focal plane of focal length f_2. The image plane scale for the two focal lengths is, of course, different; one focal plane is shown larger than the other. The chief ray makes angle α_1 with the axis for the image plane formed by focal length f_1, and the chief ray makes angle α_2 with the axis for the image plane formed at focal length f_2. As an example, we will consider a particular case. Assume that we want $Q = 2$ and that the following system parameters apply:

1. The segmented mirror has an outside diameter D of 10 m.
2. The effective focal length (EFL) of the telescope is 60 m.
3. There are no off-axis aberrations.
4. We use an 8192×8192 pixel focal plane. The FOV radius in units of pixels is given by $\sqrt{2}/2$, which equals 5,792 pixels.
5. The pixels are 4-μm pitch in size, so the FOV radius r, center to edge at the image plane is 23.2 mm.
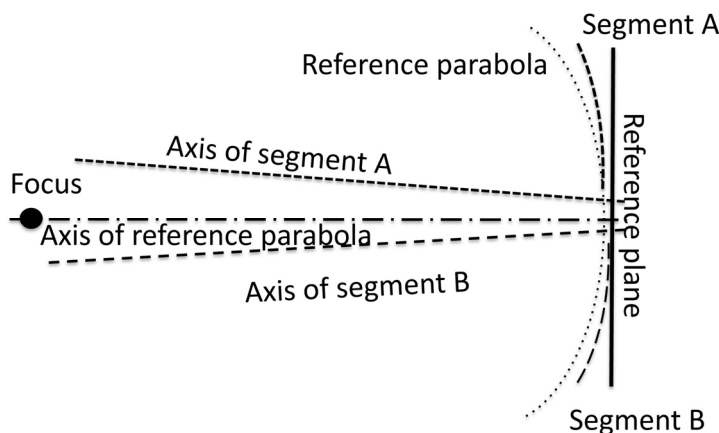
Figure 12.6 Cross-sectional diagram of a two-element segmented telescope. The reference parabola is the dotted curve with its axis passing through the desired focal point. A reference plane that also passes through the focus is shown perpendicular to the axis of the reference parabola. The misalignment of the segments is exaggerated. Segment A is shown with its axis not passing through the focus. The axis of segment B is also shown not passing through the focus.
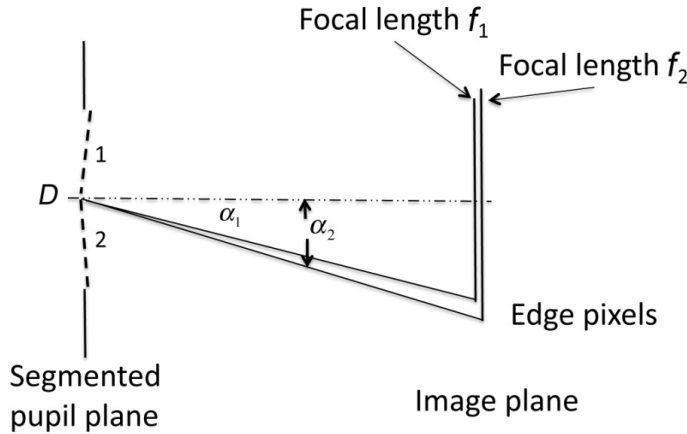
Figure 12.7 A pupil plane of diameter *D* is illuminated from the left. The pupil is segmented with two segments; the focal length of one segment is f_2, and the focal length of the second segment is f_1.

Then, the diameter *d* of the diffraction spot is given by

$$d = \frac{2.44\lambda}{D} \cdot 60 \text{ m} = 7.3 \text{ }\mu\text{m}. \qquad (12.12)$$

With 4-μm pixels, $Q \approx 2$ (for reference, see Section 9.11), and if the system is diffraction limited, the pixel sampling of the image is such that diffraction-limited images are recorded.

If r_1 and r_2 are the heights (radius from the axis to the corners) of the image for the system with focal length f_1, and for the system with focal length f_2, respectively, then we can write

$$r_1 = \alpha_1 \cdot f_1 \text{ and } r_2 = \alpha_2 \cdot f_2. \qquad (12.13)$$

If we assume that an image quality analysis allows for the 4-μm-square pixel to have an allowable error of 0.2 pixels, then the allowable shear error between the two planes is 0.8 μm at maximum, which is at the corners of the field. Therefore, the image plane scale for the system with focal length f_1 must match the image plane scale for the system with focal length f_2 to within 0.8 μm, and we can write

$$r_1 - r_2 = \Delta r = 0.8 \text{ }\mu\text{m}. \qquad (12.14)$$

From Eq. (12.13) we see that $\Delta r = \alpha_2 \cdot f_2 - \alpha_1 \cdot f_1$. It is reasonable to assume that $\alpha_1 \cong \alpha_2 \cong \alpha$; therefore,

$$\Delta r = \alpha \left(f_2 - f_1 \right). \qquad (12.15)$$

We see that if

$$\Delta r = \frac{r}{f} \cdot \Delta f, \text{ then } \Delta f = \frac{f}{r} \cdot \Delta r. \qquad (12.16)$$

Using the values given above, we find that $\Delta f = 2.07$ mm.

If we let f_k be the focal length of the kth segment, and using the term $\langle f \rangle$ to represent the focal length of the ensemble of segments, then

$$\left| \langle f \rangle - f_k \right| < 2.0 \text{ mm}. \qquad (12.17)$$

If $\left| \langle f \rangle - f_k \right| > 2.0$ mm, the PSF from one mirror is continuously changing slightly with FOV radius (relative to the other) from the field center to the field edge until, when it reaches the edge, each PSF is separated by > 0.2 pixels. In this case the OTF is not stationary across the image, and the image reconstruction algorithms we considered in Section 9.1 might not be able to reconstruct information at the diffraction limit of the telescope. At a minimum, the PSF of the system—particularly at the extremes of the FOV—is degraded, and the aperture is no longer diffraction limited. In some cases, particularly for a long-exposure recording of an image through turbulence, this may make no difference. However, for a space-based segmented telescope where diffraction-limited imaging may be desired, this is very important.

Let us assume the primary mirror to be $f/\# = 6$. For a 10-m-diameter mirror, the focal length is then 60 m, and the radius of curvature is 30 m. Therefore, to build this segmented telescope, we ask that the optician match the radii of curvature of all of the segments to within 2 mm over a distance of 60 m. It is very challenging to make the measurement and to fabricate or figure the surface of each segment to this accuracy while holding the desired mirror figure. In practice, for ground-based telescopes, these segments are either distorted slightly by providing force to warp the surface, or a correction to the wavefront is applied using the principles of two-stage optics and WFSC at a relayed image of the segmented pupil.

Many astronomical applications do not require high angular resolution but rather use the large aperture to collect photons. In this case, the radii of curvature of the segments do not need to be matched as closely as they need to be for diffraction-limited imaging performance.

Today, astronomers are moving toward very large FOVs by tiling the focal plane with array detectors. Note that as the FOV increases, the tolerance on the equality of the radii of curvature of the segments becomes tighter. Comprehensive tolerancing of a segmented telescope prior to manufacture requires setting up each segment as a separate optical system in the computer and then raytracing OPDs to the focal plane for a point on axis and points off axis.

The magnitude of misalignment that is acceptable for image quality is determined by setting up the segmented pupil with phase and amplitude errors on the complex wavefronts and iterating a reference image through the system, including appropriate signal-dependent and signal-independent noise from the detector.

12.4.2 Segmented wavefront corrector

If the second-stage optics contains a wavefront-corrector mirror that is segmented in the pattern of the primary, and if one can adjust the curvatures and the tip-tilt of each segment in this wavefront-corrector mirror, then the tolerances on the large primary mirror can be greatly reduced. However, the rotational degree of freedom and the need to co-align all of the axes of the segments with the design axis of the parent asphere of the primary as a whole must be done on the primary. Approaches to segmenting the wavefront-corrector mirror to match the primary have been suggested by several optical scientists[18] and astronomers.[19,20]

12.5 Image Quality with a Segmented Telescope

12.5.1 Image quality

Image quality from large segmented astronomical telescopes has been studied for both ground and space applications.[21–23] Studies on segmented-mirror ground astronomical telescopes have been performed assuming that the active control of tip, tilt, piston, and shape of each segment is independent of its neighbor. Analyses have been done considering the compounding effects of atmospheric turbulence.[24,25] Several groups are building segmented-telescope simulators for calculating PSFs and related metrics such as Strehl ratio, encircled energy, and MTF for both ground- and space-based segmented telescopes.

The diffraction effects for large numbers of segments were analyzed for Strehl ratio. A speckle pattern and a speckle halo were derived and observed.[22] The relationship between the number of segments and the characteristics of the multiconjugate adaptive optics system shows that the Strehl ratio is limited to 0.5–0.7 for operation in the center of the H band at 1650 nm.[26] In Section 12.5.2 we will discuss the correction of errors in segmented telescopes based on the material developed by Meinel and Meinel.[6]

12.5.2 Correcting errors in a segmented telescope with two-stage optics

The individual segments of a large lightweight segmented primary mirror have both a piston error and a tilt error. In this section we assume the segmented surface to be a rigid body, and we consider the effects on telescope system performance caused by piston errors, field-angle errors, tilt errors, and diffraction spillover. The image of the primary on the corrector is demagnified, often somewhere between a factor of 10 and 100. Field of view as a function of this demagnification is discussed in this section.

12.5.2.1 Piston error

We can use the contents of Fig. 12.8 to understand the effect of piston errors on an optical system. The lens at the prime focus images the primary mirror at the right onto a secondary mirror at the left. The piston error is shown on the primary mirror as Δz_1 and is mapped through the field lens onto the surface of the secondary mirror. The angle through which the edge ray is reflected is θ_1. The angle the ray makes with the axis after passing through the center of the field lens is θ_2. The angle between the telescope axis and a point drawn to the displaced (necessary for correction) segment on the secondary mirror is ψ.

A piston correction Δz_2 is applied at the secondary mirror. For an object on axis, it is clear that the piston error required on the secondary mirror is approximately the same magnitude but the opposite sign as the error on the primary mirror. The effect of finite slopes on the rays is small and is given by

$$\Delta z_2 \left\{ \frac{1}{\cos \theta_2} + \frac{1}{\cos \psi} \right\} = \Delta z_1 \left\{ 1 + \frac{1}{\cos \theta_1} \right\}. \qquad (12.18)$$

Rewriting this expression, we obtain

$$\Delta z_2 \approx \Delta z_1 \left[1 + \frac{1}{16F_1^2} - \frac{1}{16F_2^2} + \frac{1}{16F_3^2} \right], \qquad (12.19)$$

where F_1 is the F-number of the mirror surface 1, F_2 is the F-number of mirror surface 2, and F_3 is the F-number of mirror surface 3.
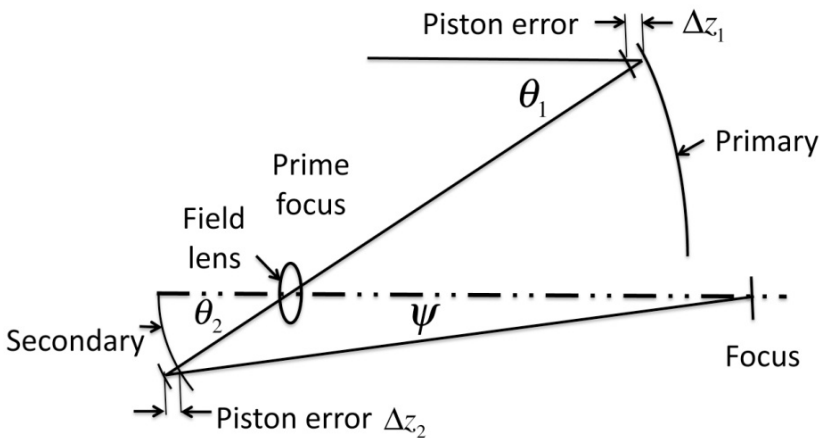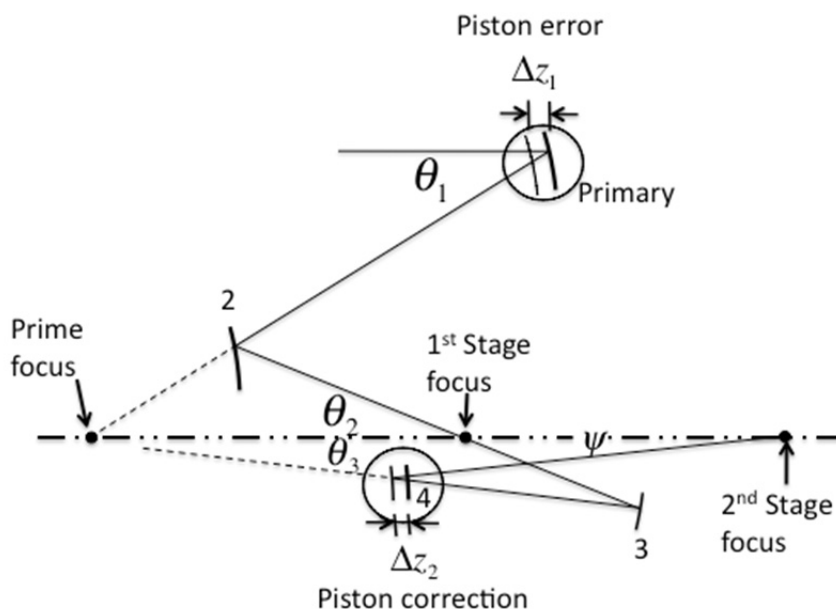

Figure 12.8 Diagram of a two-stage optical system. The large primary mirror to the right is imaged onto a secondary mirror by a field lens located at the prime focus. A given piston error on the primary mapped to the secondary is slightly different due to the angles involved. (Reprinted with permission from Ref. 6.)

12.5.2.2 Field-angle errors

Piston error also introduces field-angle errors. Often astronomers want to record images of very faint spatially extended objects using a reference star in the field from a segmented primary with piston errors. The image quality of the faint object often depends on the angular separation between the reference star used for adjusting the tip-tilt of the primary and the object. The telescope is optimized to give a good PSF at the field point where the reference star is located. Image-restoration algorithms assume that this PSF of the star is shift invariant. That is, the PSF does not change with field. If this PSF is not the same across the field, it is not isoplanatic.

   Figure 12.9 presents the geometric construction of an all-reflecting two-stage optical system that we can use for analyzing the system's ability to correct at different FOVs. The figure shows a cross-sectional view of a stage 1 Cassegrain with a piston error on a segment, followed by a stage 2 Cassegrain, which is used for correcting the piston error. The figure also shows a piston error on the primary mirror mapped through the system to the quaternary mirror. To make the angles more obvious for our analysis, Fig. 12.10 shows an enlargement of the two encircled regions in Fig. 12.9.

   Figure 12.9 shows a ray entering the system and reflecting from the segment of the primary deviated by angle θ_1. The ray continues in the direction of the prime focus but is intercepted by the convex secondary of the first stage of the two-stage

Figure 12.9 Geometric construction through a two-stage optical system showing details of the primary, secondary, tertiary, and quaternary with first- and second-stage foci identified. A piston error is shown on the primary, which is compensated by a piston correction on the quaternary. The two circles identify regions near the primary and the quaternary that are seen in the enlargement in Fig. 12.10.
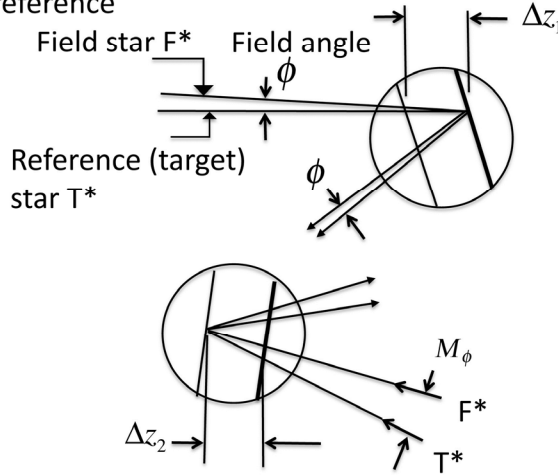
Figure 12.10 Geometric construction of rays through the two-stage optical system shown in Fig. 12.9 for the purpose of calculating the field-angle errors characteristic of compensating tilt errors in the primary by tilting a component at the image of the primary formed within the second stage.

optics concave primary mirror of the second stage. An image of the convex surface of the primary mirror is formed at the corrector element, shown as surface 4, where, to first order, the effects of piston errors on the primary are removed.

As mentioned, Fig. 12.10 shows the two regions identified inside circles in Fig 12.9. A target or reference star indicated by T* is shown. This is the star that is used for correcting and optimizing the system based on some merit function such as Strehl ratio, or to maximize the peak of the PSF. Above the target star we see a field star F*, separated in angle ϕ from the target star. The piston error Δz_1 is shown in both Figs. 12.9 and 12.10. We show the piston required to compensate the error as Δz_2. The angle between the ray for the target star and the ray for the field star has increased by a magnification factor M to become $M\phi$, where M is the ratio of the entrance pupil diameter to the exit pupil diameter (demagnification).

Examining the piston WFE in Fig 12.10, relative to the OPD for the target star, we see that there is a different, longer OPD for the field star in the first stage. The field star OPD is increased by

$$\Delta OPD = \Delta z_2 \left(\text{off-axis } OPD - \text{on-axis } OPD \right)$$

$$= \Delta z_2 \left\{ \frac{1}{\cos(\theta_2 \pm M\phi)} + \frac{1}{\cos(\psi \pm M\phi)} - \frac{1}{\cos\theta_2} - \cos\psi \right\}. \tag{12.20}$$

Note that, as drawn, the angles θ_2 and ψ are negative. Therefore, they contribute to the increase of ΔOPD in Eq. (12.20). If we let F_2 and F_3 represent the focal ratio of the primary in the second stage and the focal ratio of the final system, respectively, and we expand the cosine terms and accept terms up to ϕ^2, the OPD error becomes

$$\Delta OPD = \Delta z_2 \left\{ 1 + \frac{1}{16F_2^2} + \frac{1}{16F_3^2} \right\} M^2 \phi^2 , \qquad (12.21)$$

where M is the magnification, and ϕ is the angle between the reference star and the field star.

In Fig. 12.11 we plot the log of the fractional residual error in OPD as a function of FOV. The points related to the HST and LDR are shown. For the HST, the fractional residual error is about 5×10^{-4}. Thus, its WFE due to W_{040} of 6 waves is reduced to 0.003 waves at a field angle of 30 arcsec. Therefore, the correction provided by the second stage is excellent. For the submillimeter telescope LDR, the residual is 2×10^{-2}. Therefore, a 1-mm piston error is reduced to 2 nm or about 0.07 waves at a mean operating wavelength of 300 μm for the submillimeter telescope. The primary mirror for the LDR then has a mechanical tolerance of ±1 mm, provided a two-stage optical system is used for the telescope optics.

12.5.2.3 Tilt errors

The mirror segments of a segmented primary mirror contribute two sources of error to the whole mirror. One of these is the error in the curvature of the surface, as discussed in Section 12.4; the other is a tilt of the correct-curvature segment relative to its neighbor. Each segment contributes its own image to the image plane. If the curvature on a segment is correct, but the tilt of that segment relative to the others of the system is in error, then the image plane has two images, one from the array of correct-tilt segments as a whole, and a sheared, or displaced, image from the incorrect-tilt segment.

Figure 12.12 shows the notation we will use to describe the two-stage configuration tilt error. The upper right of the drawing shows the entrance pupil to the telescope with tilt error α. The lower left portion of the drawing shows the prime focus of the system. The ray with the error has been sheared by a distance Δy_1, and the wavefront associated with the ray arrives at the prime focus a distance Δz_1 in front of the prime focus. To the upper right of the prime focus we show the secondary mirror, which intercepts the light from the primary mirror before the prime focus. Because the secondary is curved, it adds power to the beam. At the first-stage focus, the tilted image is sheared by Δy_2, and the focal shift is Δz_2. The light proceeds through the first-stage focus to form an image of the entrance pupil, which is the same as the exit pupil. The second-stage focus is shown at the far right, where the shear is Δy_4, and the focal shift is Δz_4. In the case of the tilt of a segment, we have two effects: (1) lateral displacement of the image at the final focus and (2) a focal shift.
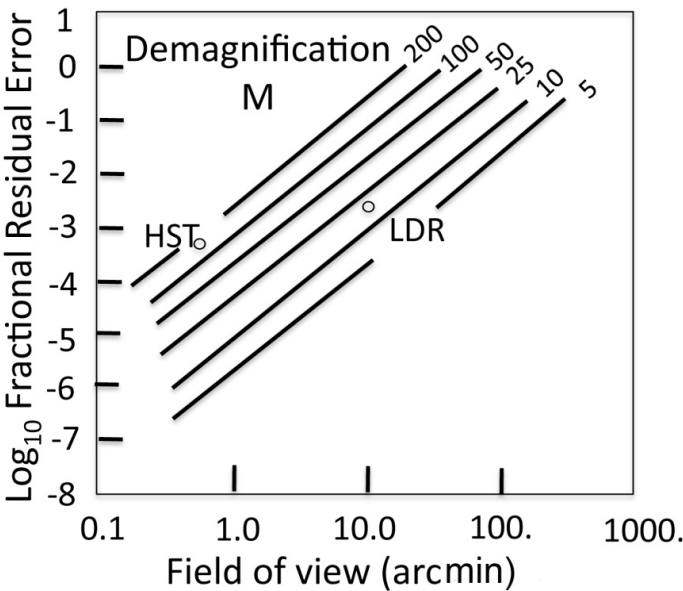
Figure 12.11 Plot showing the decrease in image quality with FOV as a function of magnification factor in the two-stage optical system. The location of the HST optics and the LDR optics are shown. (Reprinted with permission from Ref. 6.)
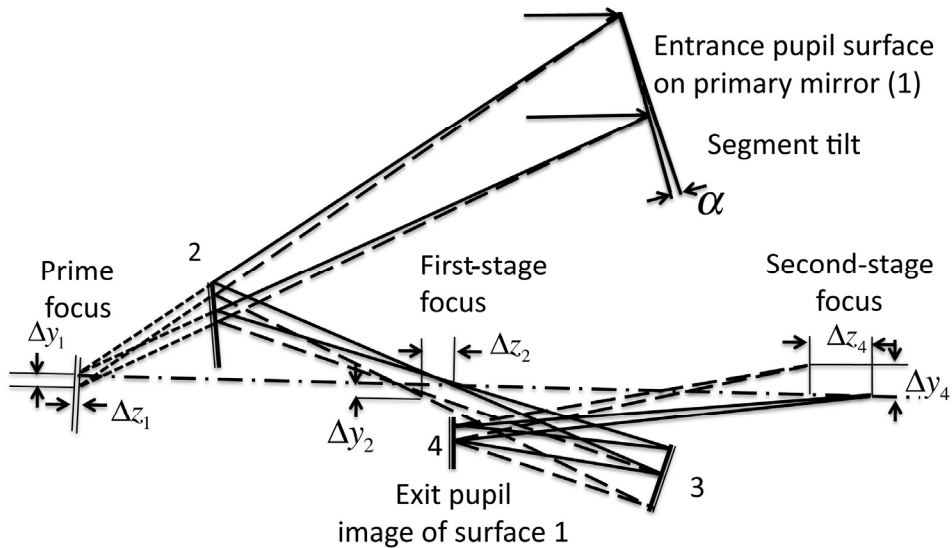
Figure 12.12 Diagram showing the notation used for calculating the error at the focal plane of the second stage caused by a tilt error in one of the segments. The mirrors are labeled in the order in which light strikes them. (Reprinted with permission from Ref. 6.)

12.5.2.4 Lateral image displacement

Characteristic of a two-stage optical system, an image of the primary is formed at the primary (the corrector optic) of the second stage. We assume that the primary of the second-stage system is segmented also and that there is a 1:1 mapping of the stage-one primary segments onto the segments of the smaller second stage. We apply the tilt correction on the segment of the second stage that is a map of the tilted error on the primary.

The equation for a tilt correction γ_3 for the lateral displacement of the image in the final focal plane due to a segment tilt α is seen to be approximately

$$\gamma_3 = \alpha \frac{P_1}{P_3} = \alpha \frac{F_{sys}}{F_1} = \alpha M, \qquad (12.22)$$

where P_1 is the diameter of the entrance pupil, P_3 is the diameter of the exit pupil, F_{sys} is the focal ratio of the system, F_1 is the focal ratio of the first stage, and M is the demagnification of the pupils.

12.5.2.5 Focal shift

The equation whereby piston is corrected to compensate for the defocus of the final image caused by segment tilt is approximately

$$\Delta z_4 = \frac{a D F_{sys}^2}{F_1} = a D M^2, \qquad (12.23)$$

where D is the diameter of the telescope. Note that the correction goes as the square of the demagnification. The dependence of the correction ratio on refocus correction, piston error, and angle correction are shown in Fig. 12.13. This figure gives the relationship between the tilt and piston corrections and the refocus for a mirror segment as a function of demagnification M for a 1-m-diameter primary mirror:

$$\text{Line A is the ratio } \frac{\text{angle of correction (arcsec)}}{\text{input angle error (arcsec)}}.$$

$$\text{Line B is the ratio } \frac{\text{piston correction (mm)}}{\text{input piston error (mm)}}.$$

$$\text{Line C is the ratio } \frac{\text{correction refocus (mm)}}{\text{input angle error (arcsec)}}.$$
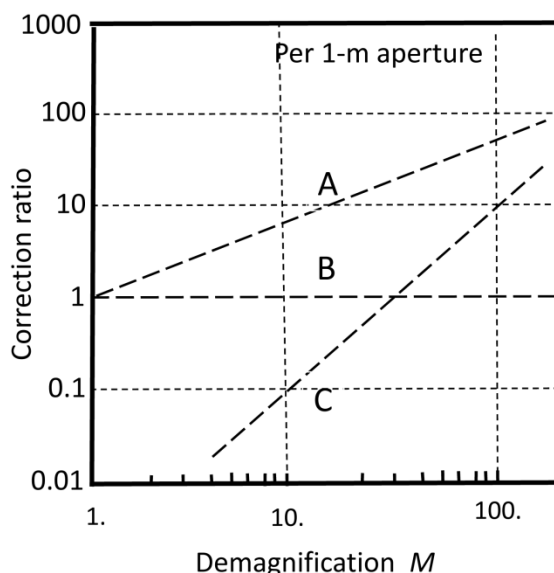
Figure 12.13 Plot showing the relationship between the piston and tilt corrections and the refocus for a mirror segment as a function of demagnification *M* for a 1-m diameter primary mirror. The numbers are scaled linearly for other aperture sizes. (Reprinted with permission from Ref. 6.)

12.6 Effects of Gaps on Image Quality

Because gaps exist between the segments to allow folding the mirror to package it in a volume smaller than is required for a large aperture, a characteristic diffraction pattern appears at the image plane; if regular hexagonal segments are used, the PSF is a six-pointed star. If A_F represents the area of the filled aperture and A_S represents the surface area of the segments, then the proportion of energy E_P outside the core PSF is given by

$$E_p = \frac{A_F - A_S}{A_F}. \tag{12.24}$$

To control the scattered light introduced by the segment edges when building an astronomical coronagraph for low-contrast observations, one may need to apodize each segment separately by relaying the hexagonally segmented pupil onto a mask.

Image quality in the thermal IR requires an understanding of all thermal noise sources in the system. The areas in the gaps between the mirror segments are a potential source of unwanted background radiation and need to be considered when calculating noise sources. Gaps in the segments also require nonconventional adaptive optics and create interesting challenges for the exoplanet-characterization community.[27,28]

12.7 The James Webb Space Telescope (JWST)

In an earlier section we learned that current space telescopes, for example, JWST, use lightweight advanced materials to segment the primary mirror and fold it to reduce launch volume. The segments are machined and figured from a billet of beryllium. Beryllium has a low density of 1850 kg/m^3, with a Young's modulus of 300 GPa, Poisson ratio of 0.08, and a low coefficient of expansion of 0.05 at the operating temperature of the JWST (40 K). The thermal conductivity is high (210 W/mK), enabling the mirror to quickly come to thermal equilibrium. Ground-based segmented telescopes use borosilicate glass, or low-coefficient-of-thermal-expansion glasses (e.g., ULE® or Zerodur®).

Figure 12.14 shows a hexagonally segmented mirror with two rings. In theory, there is no limit to the number of rings that can be used for an astronomical telescope. The tradeoff is between mechanical complexity, metrology, and segment cost. JWST uses two rings of segments. Figure 12.15 shows fold lines for the deployment of JWST.
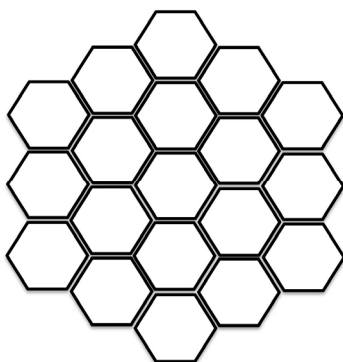
Figure 12.14 Hexagonal layout for the 18-segment 6-m JWST.
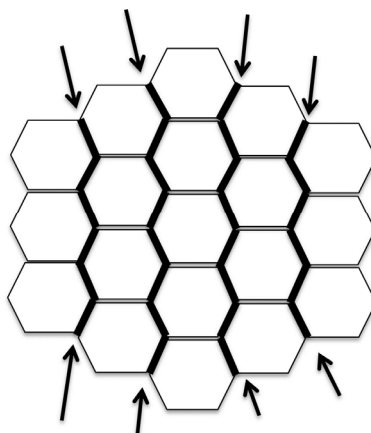
Figure 12.15 Hexagonal layout for the JWST, including the fold lines.

12.8 Giant Ground-based Telescopes

The Twin Keck Telescopes were the first successful large-aperture (10 m each) segmented telescopes. Details of these telescopes are found at www.keckobservatory.org and is not repeated here.

The Thirty Meter Telescope (TMT) project is a partnership between Caltech, the University of California, and the Association of Canadian Universities for Research in Astronomy to develop a 30-m-diameter optical telescope. The National Astronomical Observatory of Japan is a collaborating institution. Detailed studies have been completed for trading off segment size, control requirements, and scientific performance.[10] The TMT will employ a laser guide star / adaptive optics system that will enable the telescope to image near the diffraction limit. The system will generate six sodium laser beams. The conceptual design is based on three 25-W solid-state continuous wave, sum frequency 589-nm lasers. The alignment and phasing system has 12,000 degrees of freedom.[29] Details on the TMT are found at www.tmt.org. Details of the Giant Magellan Telescope[30] (GMT) are found at www.gmto.org. Details of the European Extremely Large Telescope[31] (E-ELT) are found at www.eso.org/public/astronomy/teles-instr/e-elt.html.

References

1. G. Agapito, S. Baldi, G. Battistelli, et al., "Automatic tuning of the internal position control of an adaptive secondary," *Europ. J. Control* **17**(3), 273–289 (2001).

2. E. Hugot, M. Ferrari, A. Riccardi, et al. "Stress polishing of thin shells for adaptive secondary mirrors: Application to the Very Large Telescope secondary," *Astron. & Astrophys*. **527**, A4, March (2011).

3. H. P. Stahl, "Survey of cost models for space telescopes," *Opt. Eng*. **49**(5), 053005 (2010) [doi: 10.1117/1.3421681].

4. S. J. Thompson, A. P. Doel, D. Brooks, and M. Strangwood, "Toward a large lightweight mirror for AO: Development of a 1-m Ni-coated CFRP mirror," *Proc. SPIE* **7018,** 701839 (2008) [doi: 10.1117/.12.786079].

5. A. Riccardi, G. Brusa, P. Salinari, D. Gallieni, R. Biasi, M. Andrighettoni, and H. M. Martin, "Adaptive secondary mirrors for the Large Binocular Telescope" *Proc. SPIE* **4839**, 721–732 (2003) [doi: 10.1117/12.458961].

6. A. Meinel and M. P. Meinel, "Two-stage optics: high-acuity performance from low-acuity optical systems," *Opt. Eng.* **31**(11), 2271–2281 (1992) [doi:10.1117/12.59946].

7. J. L. Fanson, "On the use of electrostrictive actuators in recovering the optical performance of the Hubble Space Telescope," *Materials for Smart Systems Proceedings 1994*, p. 109, Materials Research Society (1995).

8. R. L. Plante, "Large Active Mirror Program (LAMP)," *Proc. SPIE* **1543**, 146–160 (1992) [doi: 10.1117/12.51177].

9. P. Y. Bely, Ed., *The Design and Construction of Large Optical Telescopes*, Astronomy and Astrophysics Library, Springer-Verlag, New York, p. 153, (2003).

10. C. Baffes, T. Mast, J. Nelson, et al., "Primary mirror segmentation studies for the Thirty Meter Telescope," *Proc. SPIE* **7018**, 70180S (2008) [doi: 10.1117/12.790206].

11. W. R. Ogerele, L. D. Feinberg, L. R. Purves, et al. "ATLAST"-9.2m: a large aperture deployable space telescope," *Proc. SPIE* **7731**, [doi: 10.1117/12.857622] (2010).

12. H. P. Stahl, H. Thronson, S. Langhoff, M. Postman, D. Lester, C. Lillie, and R. J. Brissenden "Potential astrophysics science missions enabled by NASA's planned Ares V," *Proc. SPIE* **7436**, (2009) [doi: 10.1117/12.826748].

13. J. Nelson, T. Mast, and G. Chanan, "Aberration correction in a telescope with a segmented primary," *Proc. SPIE* **1114**, 241–257 (1989).

14. P. Wizinowich, T. Mast, J. Nelson, and M. DiVittorio, "Optical quality of the W. M. Keck Telescope," *Proc. SPIE* **2199**, 94–104 (1994) [doi: 10.1117/12.176164].

15. G. A. Chanan, C. Ohara, and M. Troy, "Phasing the mirror segments of the Keck Telescopes: the narrow band phasing algorithm," *Appl. Opt*. **39**, 4706–4714 (2000).

16. G. Chanan, M. Troy, and S. Isabelle, "Fresnel phasing of segmented mirror telescopes," *Appl. Opt*. **50**, 6283–6293 (2011).

17. D. Cheng, Y. Wang, M. M. Talha, J. Chang, and H. Hua, "Effect of radius mismatch on performance of segmented telescope systems," *Proc. SPIE* **6834**, 68341Y (2007) [doi: 10.1117/12.754674].

18. V. F. Canales, J. E. Oti, P. J. Valle, M. P. Cagigal, and N. Devaney, "Reduction of the diffraction pattern in segmented apertures" *Opt. Eng*. **45**, 098001 (2006) [doi: 10.1117/1.2354160].

19. C. F. Lillie, M. Flannery, and D. Dailey "Segmented telescopes for coronagraphs," *Proc. SPIE* **5487**, 1376–1382 (2004) [doi: 10.1117/12.552348].

20. P. Martinez, A. Boccaletti, M. Kasper, C. Cavarroc, N. Yaitskova, T. Fusco, and C. Verinaud, "Comparison of coronagraphs for high contrast imaging in the context of Extremely Large Telescopes" *Astron. & Astrophys*. **492**, 289–300 (2008).

21. A. Schumacher, N. Delaney, et al., "Phasing segmented mirrors: a modification of the Keck narrow-band technique and its application to extremely large telescopes,"*Appl. Opt.* **41**(41), 1297–1307 (2002).

22. N. Yaitskova, K. Dohlen, and P. Dierickx "Analytical study of diffraction effects in extremely large segmented telescopes" *J. Opt. Soc. Am.* **20** 1563–1574 (2003)

23. D. O'Donoghue, E. Atad-Ettedgu, et al., "The image quality of the South African Large Telescope (SALT)," *Proc. SPIE* **7018**, 701813 (2008) [doi: 10.1117/12.788841].

24. N. Yaitskova and K. Dohlen, "Simulation of imaging performance for extremely large segmented telescopes," *Proc. SPIE* **4003**, 279–290 (2000) [doi: 10.1117/12.391517].

25. N. Yaitskova and K. Dohlen, "Tip-tilt error for extremely large segmented telescopes: detailed theoretical point spread function analysis and numerical simulation results," *J. Opt. Soc. Am. A* **19**, 1274–1285 (2002).

26. L. Jolissaint and J.-F. Lavigne, "An analytic model for the study of the impact of mirror segmentation on AO performance, and application to a 30-meter telescope," *Proc. SPIE* **5497**, 349–360 (2004) [doi: 10.1117/12.552551].

27. N. Yaitskova "Adaptive optics correction of segment aberration," *J. Opt. Soc. Am.* **26**, 59–71 (2009).

28. S. Remi, P. Laurent, F. Andre, et al. "Apodized pupil Lyot coronagraphs for arbitrary apertures II. Theoretical properties and application to extremely large telescopes," *Astroph. J.*, 695–706 (2009).

29. M. Troy, G. Chanan, et al., "A conceptual design for the Thirty Meter Telescope alignments and phasing system," *Proc. SPIE* **7012**, 70120Y (2008) [doi: 10.1117/12.788560].

30. Johns, M., "Progress on the GMT," *Proc. SPIE* **7012**, 70121B (2008) [doi: 10.1117/12.788063].

31. R. Gilmozzi and J. Spyromilio, "The 42m European ELT: Status," *Proc. SPIE* **7012**, 701219 (2008) [doi: 10.1117/12.790801].

Bibliography

Alloin, D. M., *Diffraction-limited Imaging with Very Large Telescopes*, Kluwer, Dordrecht and Boston (1989).

Bely, P. Y., Ed., *The Design and Construction of Large Optical Telescopes*, Astronomy and Astrophysics Library, Springer-Verlag, New York (2003).

Cheng, J., *The Principles of Astronomical Telescope Design*, Springer Science+Business Media, New York (2009).

Schroeder, D. J., *Astronomical Optics*, Academic Press, San Diego (2000).

Wilson, R. N., *Reflecting Telescope Optics II: Manufacture, Testing, Alignment, Modern Techniques*, Astronomy and Astrophysics Library, Springer-Verlag, Berlin-Heidleberg (1996).